Article

One-dimensional Luttinger liquids in a two-dimensional moiré lattice

Pengjie Wang[1,10], Guo Yu[1,2,10], Yves H. Kwan[3,10], Yanyu Jia[1], Shiming Lei[4,5], Sebastian Klemenz[4,6], F. Alexandre Cevallos[4], Ratnadwip Singha[4], Trithep Devakul[7], Kenji Watanabe[8], Takashi Taniguchi[9], Shivaji L. Sondhi[1,3], Robert J. Cava[4], Leslie M. Schoop[4], Siddharth A. Parameswaran[3] & Sanfeng Wu[1]✉

The Luttinger liquid (LL) model of one-dimensional (1D) electronic systems provides a powerful tool for understanding strongly correlated physics, including phenomena such as spin–charge separation[1]. Substantial theoretical efforts have attempted to extend the LL phenomenology to two dimensions, especially in models of closely packed arrays of 1D quantum wires[2–13], each being described as a LL. Such coupled-wire models have been successfully used to construct two-dimensional (2D) anisotropic non-Fermi liquids[2–6], quantum Hall states[7–9], topological phases[10,11] and quantum spin liquids[12,13]. However, an experimental demonstration of high-quality arrays of 1D LLs suitable for realizing these models remains absent. Here we report the experimental realization of 2D arrays of 1D LLs with crystalline quality in a moiré superlattice made of twisted bilayer tungsten ditelluride ($tWTe_2$). Originating from the anisotropic lattice of the monolayer, the moiré pattern of $tWTe_2$ hosts identical, parallel 1D electronic channels, separated by a fixed nanoscale distance, which is tuneable by the interlayer twist angle. At a twist angle of approximately 5 degrees, we find that hole-doped $tWTe_2$ exhibits exceptionally large transport anisotropy with a resistance ratio of around 1,000 between two orthogonal in-plane directions. The across-wire conductance exhibits power-law scaling behaviours, consistent with the formation of a 2D anisotropic phase that resembles an array of LLs. Our results open the door for realizing a variety of correlated and topological quantum phases based on coupled-wire models and LL physics.

Journal club Zumbühl Group
Henok Weldeyesus

12.05.2023

Outline

- Introduction
  - Luttinger liquid
  - Coupled wire models
- One dimensional Luttinger liquids in a two-dimensional moire lattice

The Luttinger liquid (LL) model of one-dimensional (1D) electronic systems provides a powerful tool for understanding strongly correlated physics, including phenomena such as spin–charge separation[1]. Substantial theoretical efforts have attempted to extend the LL phenomenology to two dimensions, especially in models of closely packed arrays of 1D quantum wires[2–13], each being described as a LL. Such coupled-wire models have been successfully used to construct two-dimensional (2D) anisotropic non-Fermi liquids[2–6], quantum Hall states[7–9], topological phases[10,11] and quantum spin liquids[12,13]. However, an experimental demonstration of high-quality arrays of 1D LLs suitable for realizing these models remains absent. Here we report the experimental realization of 2D arrays of 1D LLs with crystalline quality in a moiré superlattice made of twisted bilayer tungsten ditelluride ($tWTe_2$). Originating from the anisotropic lattice of the monolayer, the moiré pattern of $tWTe_2$ hosts identical, parallel 1D electronic channels, separated by a fixed nanoscale distance, which is tuneable by the interlayer twist angle. At a twist angle of approximately 5 degrees, we find that hole-doped $tWTe_2$ exhibits exceptionally large transport anisotropy with a resistance ratio of around 1,000 between two orthogonal in-plane directions. The across-wire conductance exhibits power-law scaling behaviours, consistent with the formation of a 2D anisotropic phase that resembles an array of LLs. Our results open the door for realizing a variety of correlated and topological quantum phases based on coupled-wire models and LL physics.

Introduction

Fermi liquid theory

- Low temperature description of many metals
- Interacting electrons → non-interacting quasi particle excitations

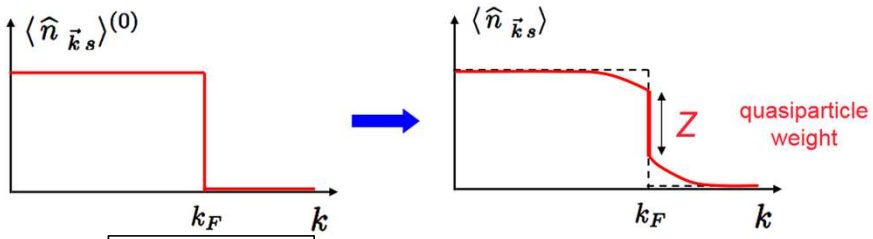

Turn on the interactions

Lecture notes: Solid state theory Manfred Sigrist 2014

Luttinger Liquids

- Fermi liquid theory breaks down in 1d
- Correct low energy model is Tomonaga luttinger liquid
  - Dispersion is linearized around Fermi points
  - Two collective excitations (Spin-charge Separation)
    - Charge
    - Spin

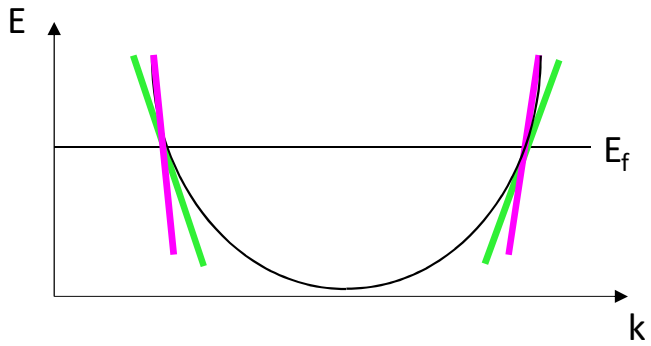

Charecteristic power-law behavior for tunneling:

$$G \propto T^{\alpha}$$
$$G \propto V^{\beta}$$

With $\alpha = \beta$

Coupled wire models

Previous works:

Two-Dimensional Anisotropic Non-Fermi-Liquid Phase of Coupled Luttinger Liquids

Ashvin Vishwanath[1] and David Carpentier[2]
[1]*Physics Department, Princeton University, Princeton, New Jersey 08544*
[2]*Institute for Theoretical Physics, University of California, Santa Barbara, California 93106-4030*
(Received 14 March 2000)

Sliding Luttinger liquid phases

Ranjan Mukhopadhyay, C. L. Kane, and T. C. Lubensky
Department of Physics, University of Pennsylvania, Philadephia, Pennsylvania 19104
(Received 8 February 2001; published 9 July 2001)

Fractional Quantum Hall Effect in an Array of Quantum Wires

C. L. Kane, Ranjan Mukhopadhyay, and T. C. Lubensky
Department of Physics and Astronomy, University of Pennsylvania, Philadelphia, Pennsylvania 19104
(Received 27 August 2001; published 4 January 2002)

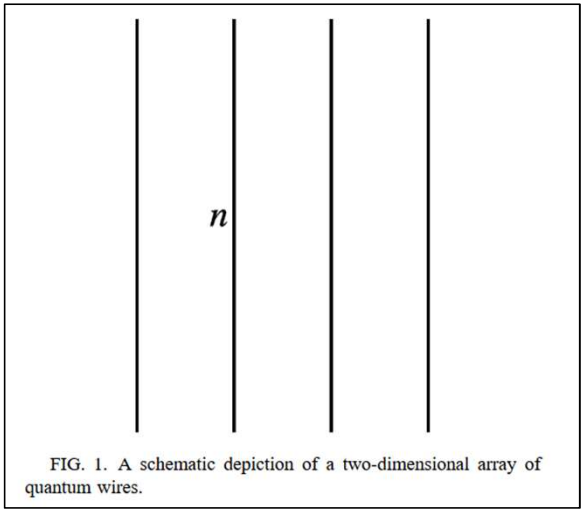

FIG. 1. A schematic depiction of a two-dimensional array of quantum wires.

Coupled wire models

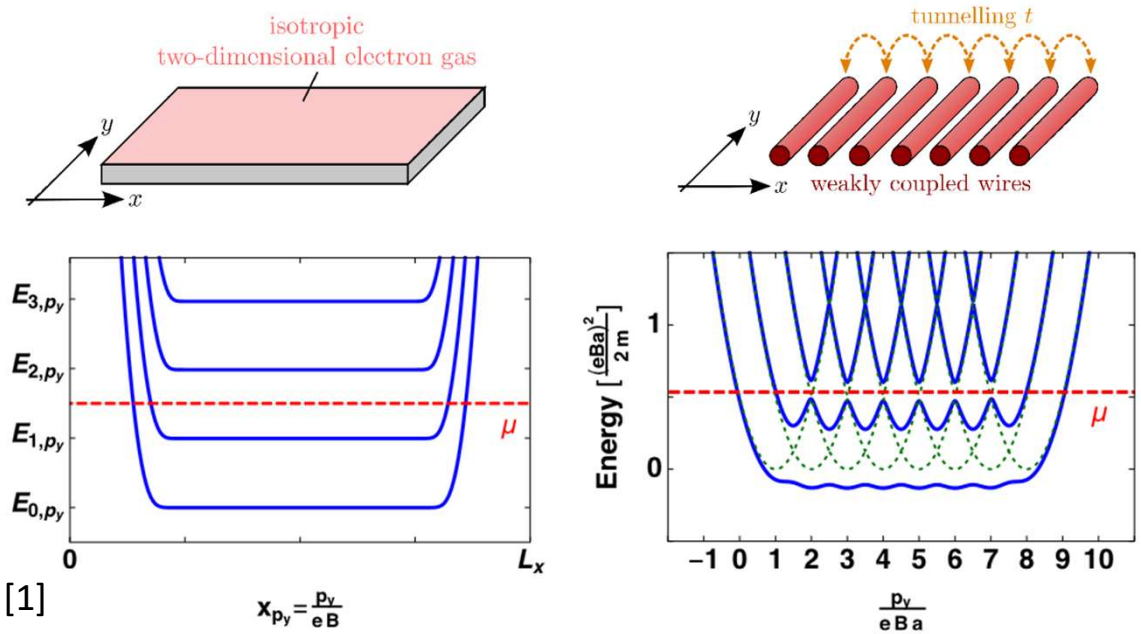

[1]

[1] *Tobias Meng ,* Eur. Phys. J. Special Topics 229, 527–543 (2020)

Coupled wire models

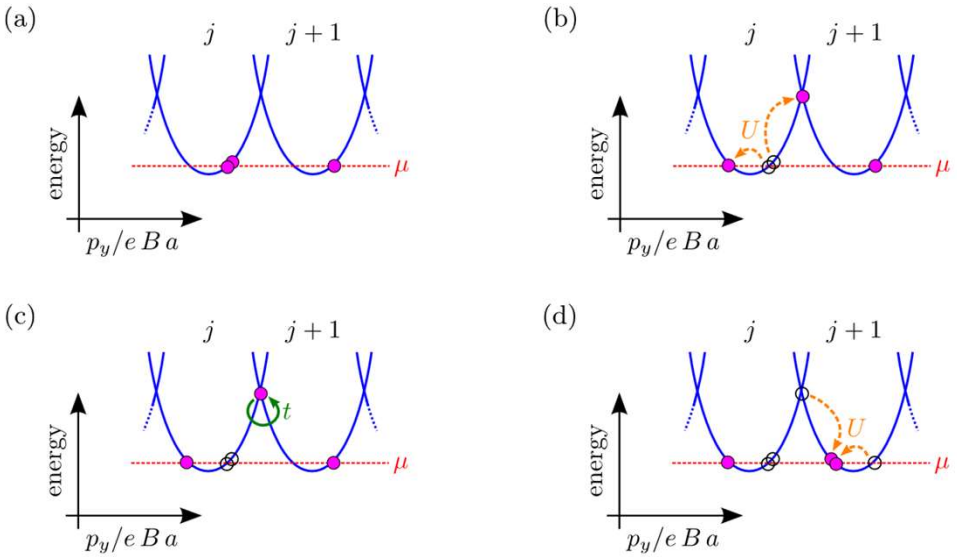

[1]

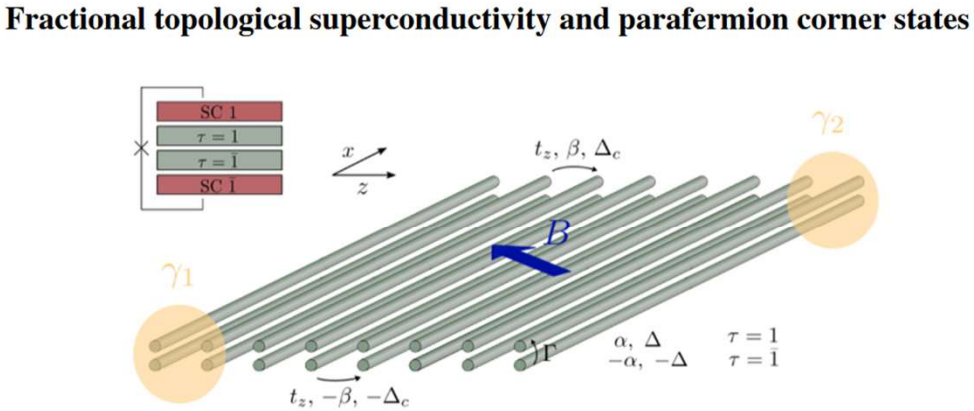

[2]

[1] *Tobias Meng* , Eur. Phys. J. Special Topics 229, 527–543 (2020)

[2] *Katharina Laubscher, Daniel Loss, and Jelena Klinovaja,* Phys. Rev. Research 1, 032017(R)(2019)

This work

Fabrication

Bottom structure

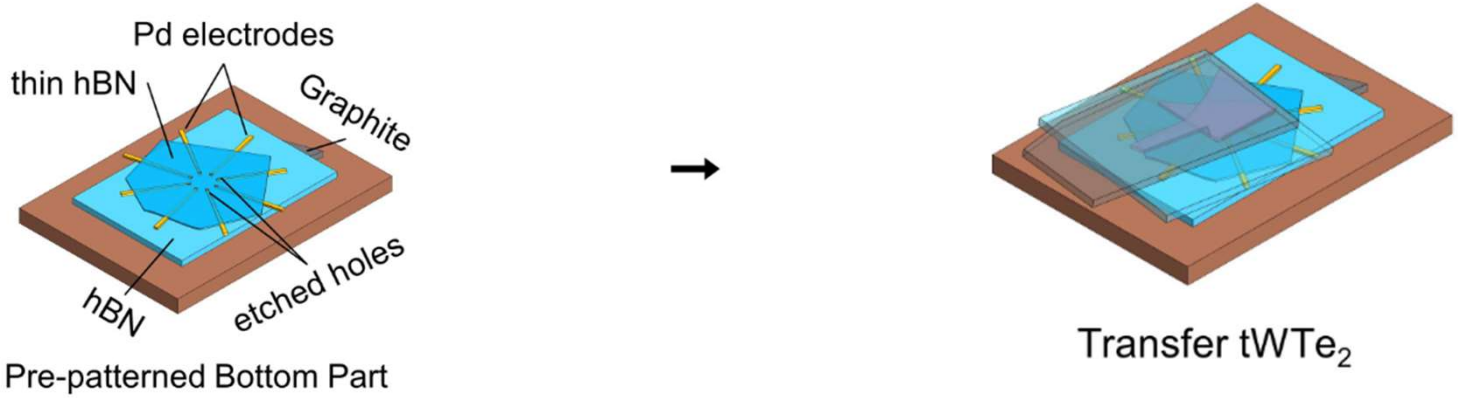

tWTe2 stack

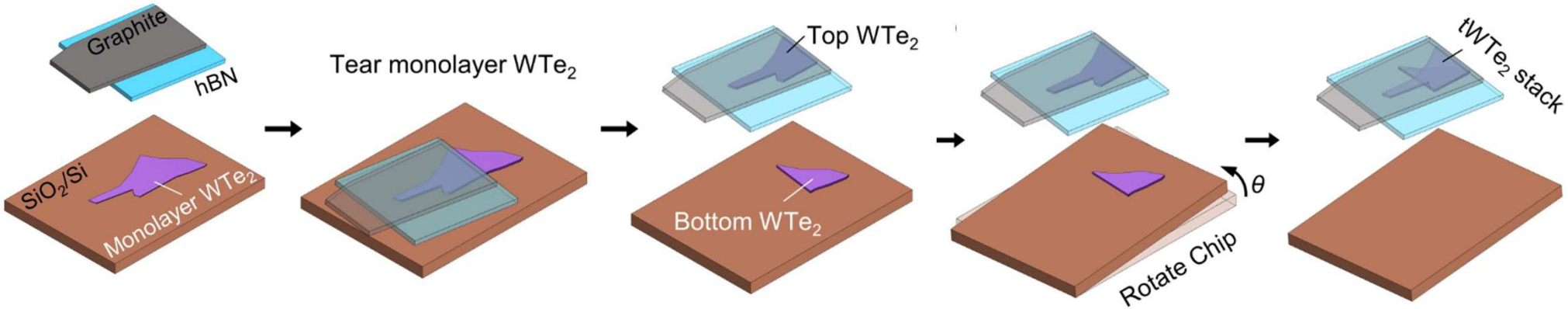

Moire Structure

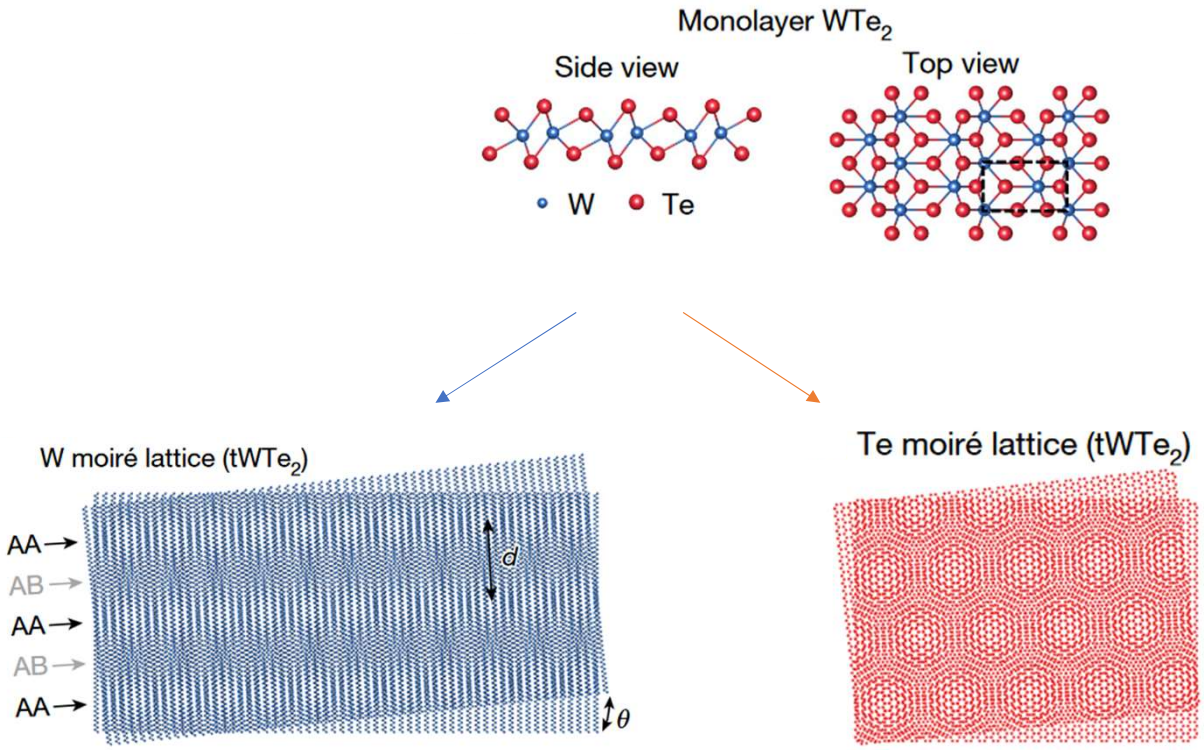

Structural analysis

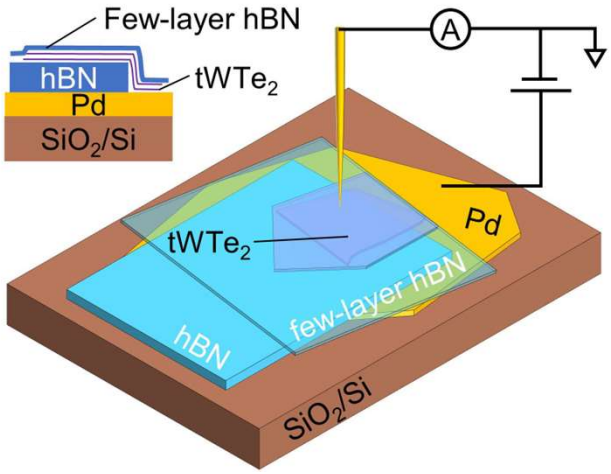

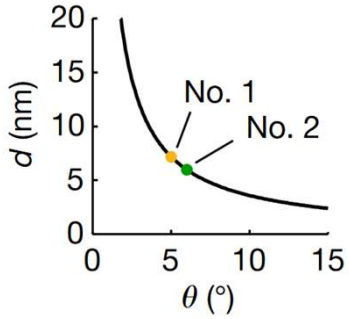

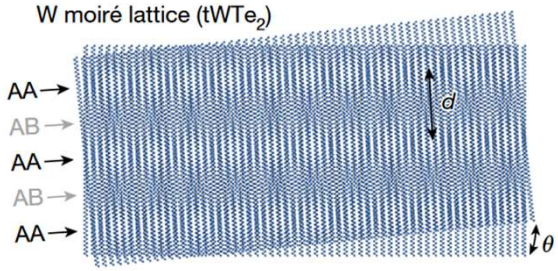

Conductive AFM

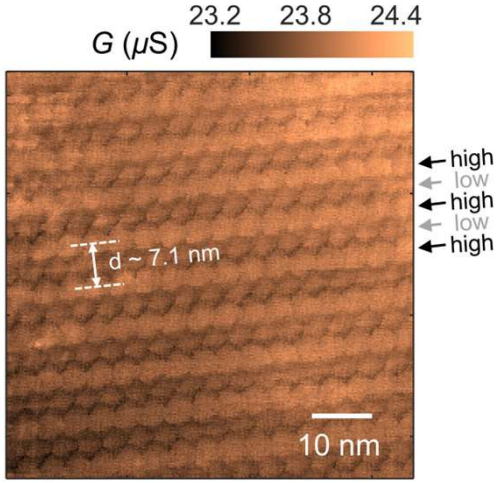

Resistance anisotropy

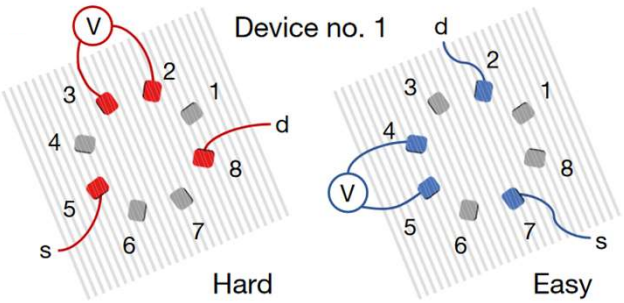

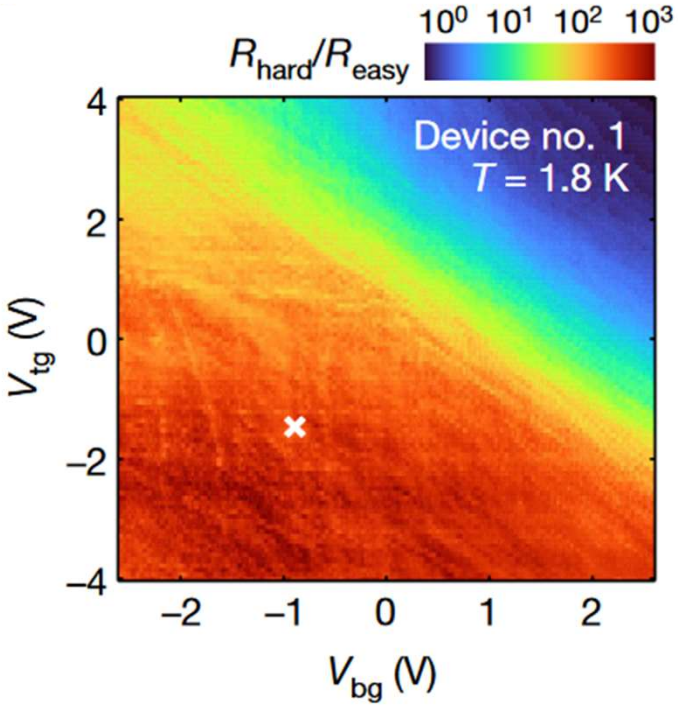

Across-wire transport

- Power-law in dc-Bias voltage
- Universal scaling
- Same exponent for Vsd and T sweeps

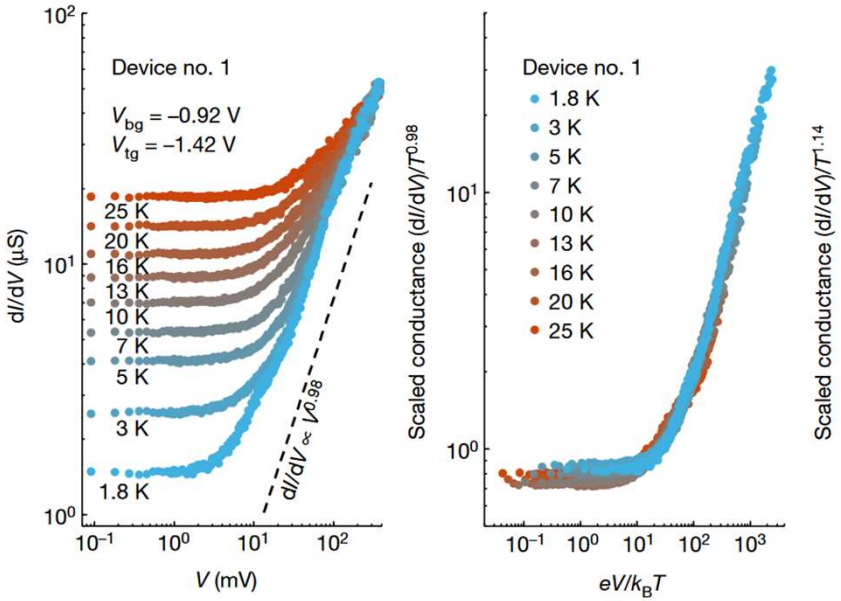

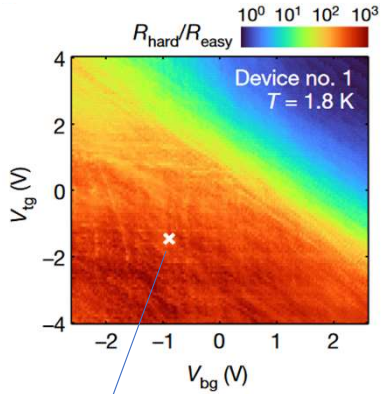

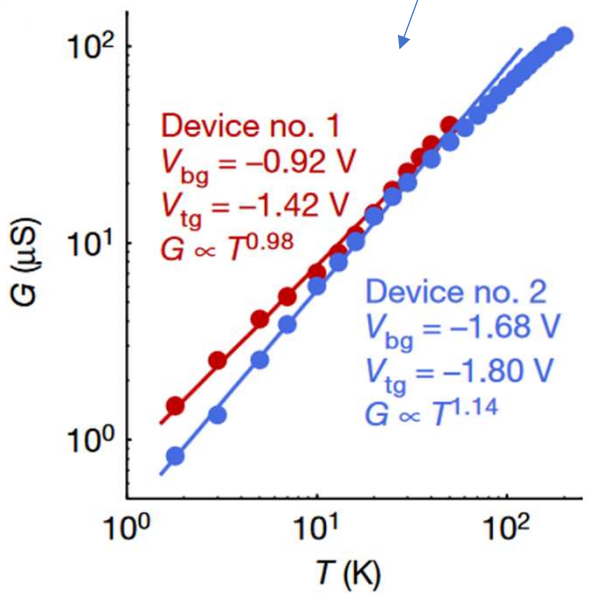

Doping dependence of power-law exponent

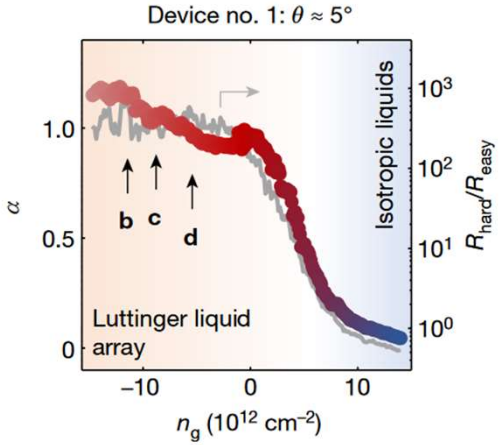

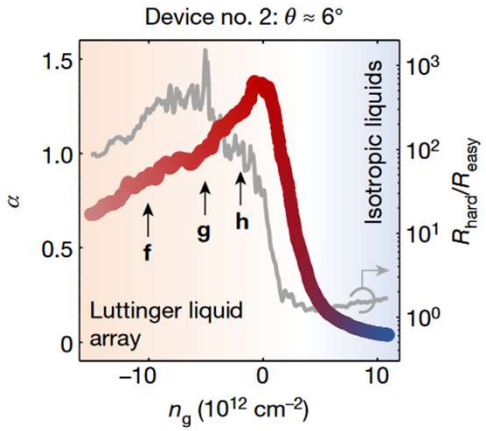

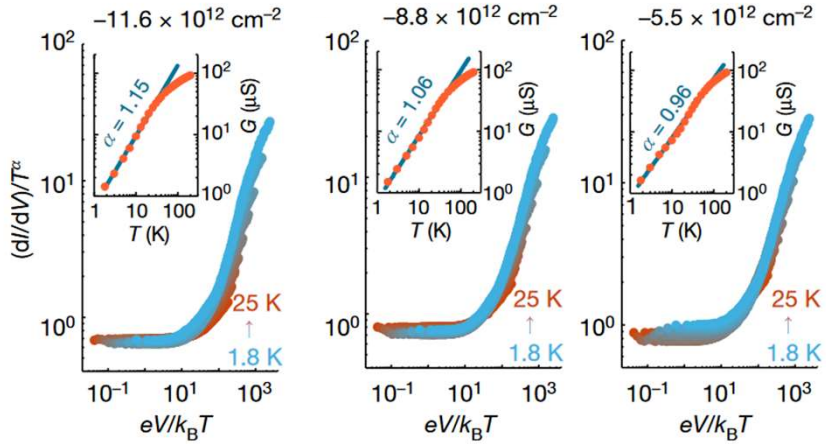

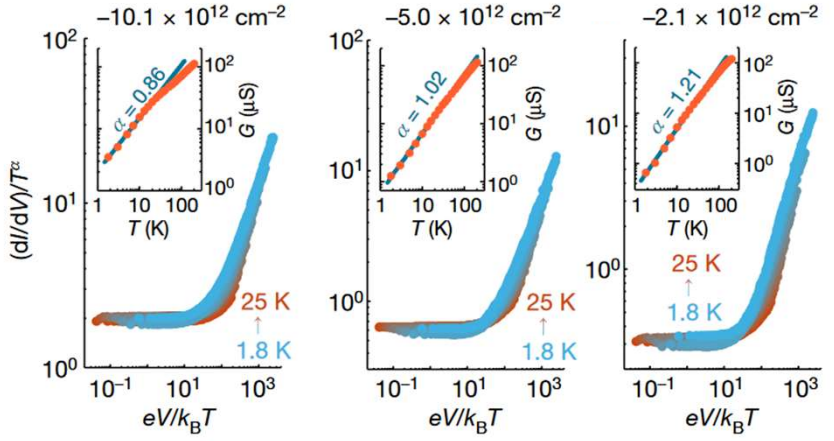

Why across wire transport?

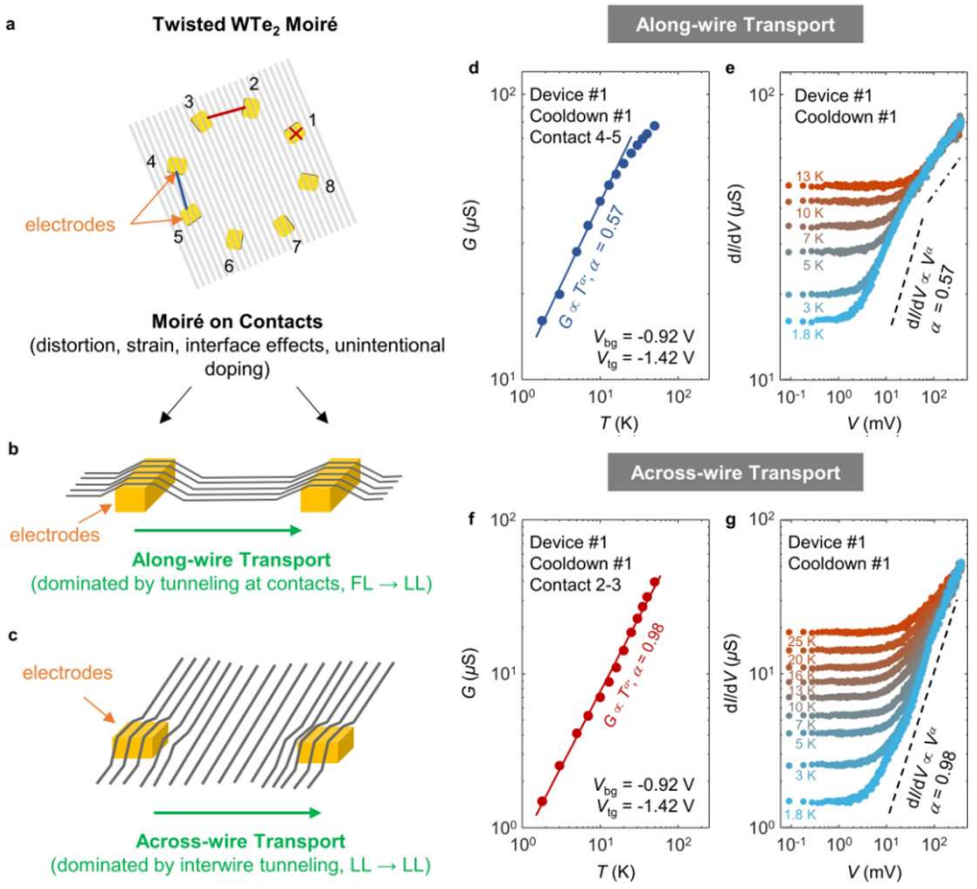

Summary

- First realization of parallel 1d wire array on the nanoscale
- Signs of Luttinger liquid behavior
  - Tunable power-law exponent (tunable interactions?)

- Future:
  - New quantum hall states
  - Spin –charge separation in 2D

appendix

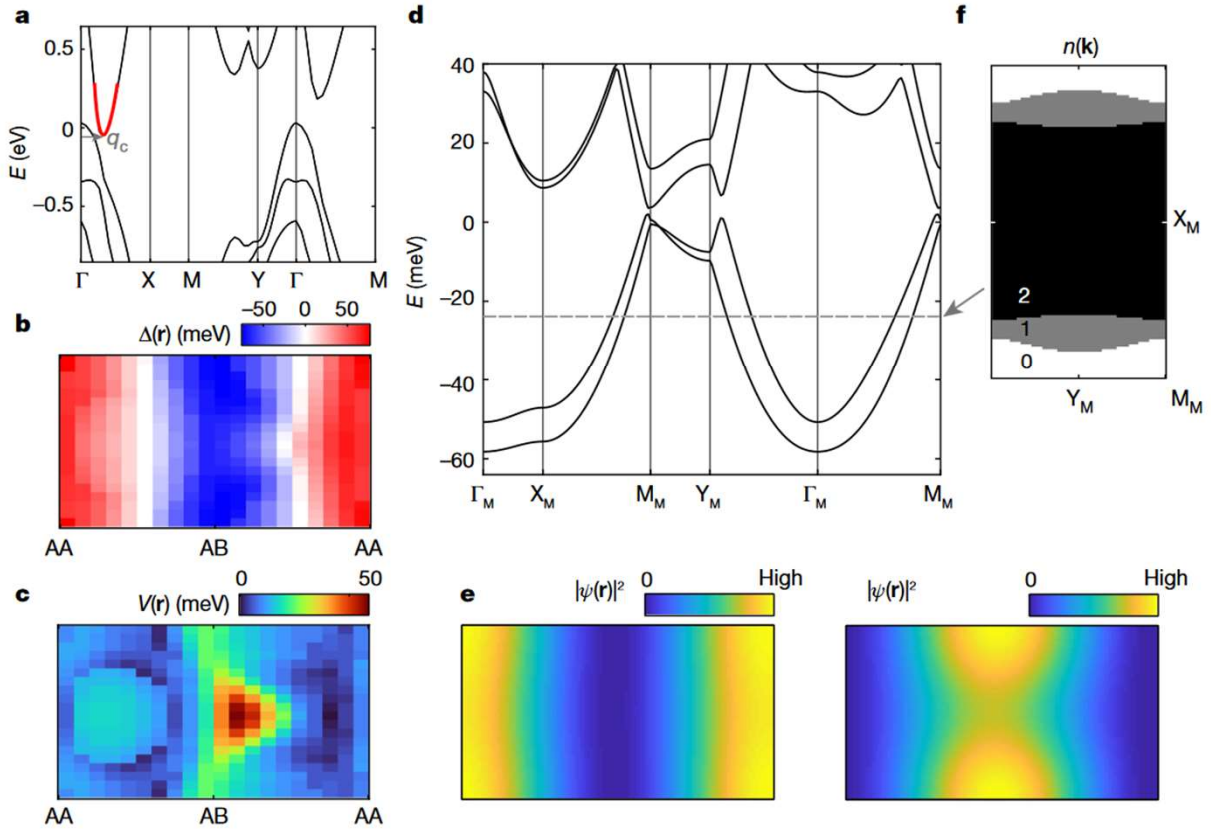

Fig. 4 | Theoretical modelling and the emergence of quasi-1D moiré bands at the single-particle level. a, DFT band structure for monolayer WTe_2. Red shading highlights the conduction band valleys at $\pm q_c$, about which the continuum model analysis in **b**–**f** is performed. Results are shown for one of the valleys. Energies are measured relative to the Fermi energy at charge neutrality. **b**,**c**, Interlayer hopping (**b**) and potential terms (**c**) plotted in the moiré unit cell. These quantities are extracted from DFT calculations of untwisted bilayers with in-plane shift $\mathbf{d} \approx \theta \hat{z} \times \mathbf{r}$, valid for a rigidly twisted $tWTe_2$. AA and AB indicate the positions of W superlattice chains (see Fig. 1b). **d**, Continuum model band structure for a conduction band valley, plotted along a cut in the moiré BZ. On hole doping, the system enters a highly anisotropic regime induced by the moiré physics. **e**, Representative Bloch wavefunctions in the quasi-1D regime plotted in the moiré unit cell. **f**, Illustrations of the quasi-1D open Fermi surfaces for moderate hole doping, with the number of occupied quasi-1D bands indicated.

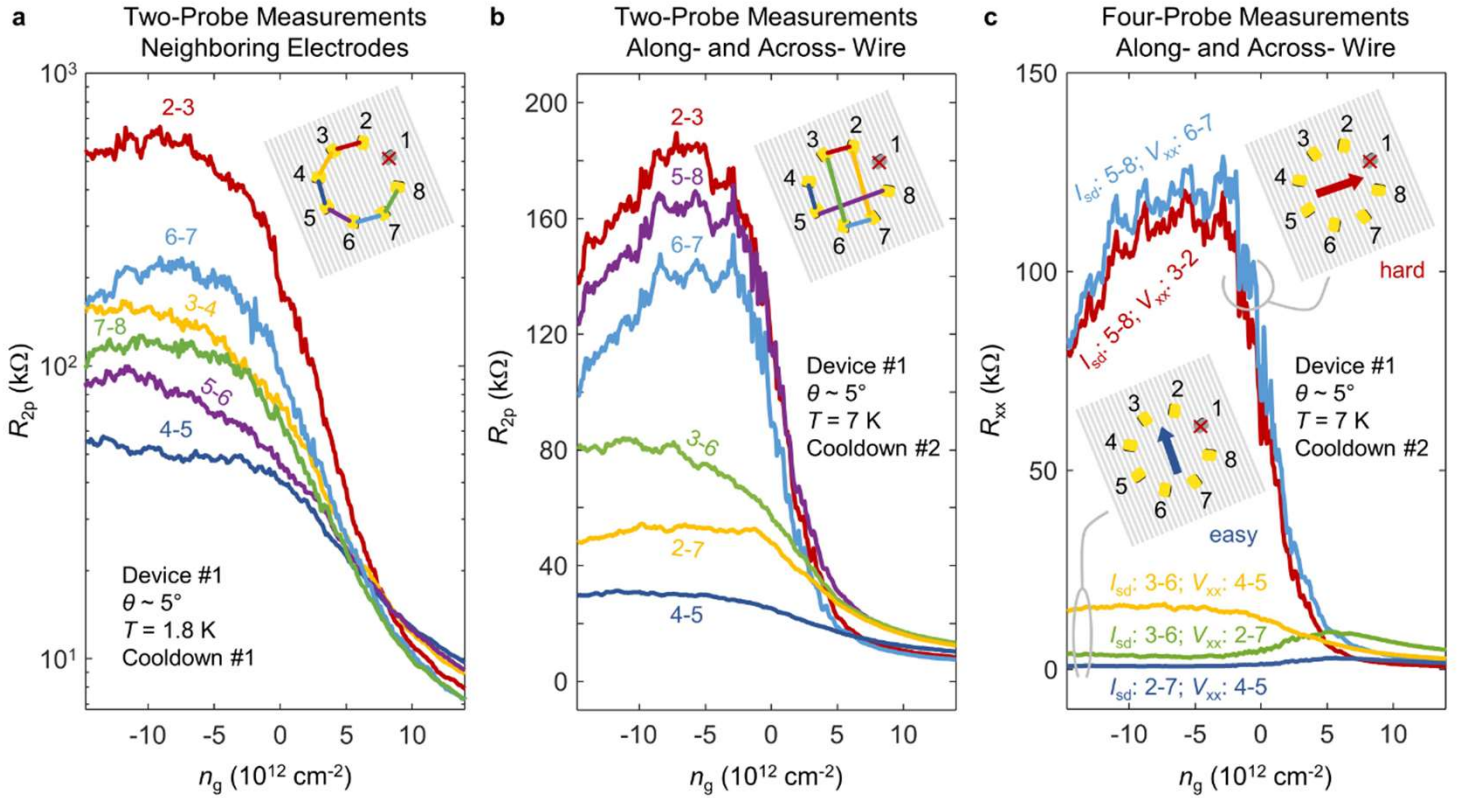

Extended Data Fig. 3 | More analysis on the transport anisotropy on device no. 1. a, Two-probe resistance between neighbouring electrodes as a function of n_g in cooldown no. 1. Inset shows the contact configurations for each measurement, where the estimated hard direction (stripe direction) is indicated by the grey lines (not to scale). $R_{2\text{-}3}$ and $R_{6\text{-}7}$ display larger values than all others in the hole-doped regime, signifying the hard direction, whereas $R_{4\text{-}5}$ shows the lowest value. Contact 1 was broken during the fabrication. The contact resistance plays a significant role here. After the easy and hard directions were identified, we performed four-probe measurements, as shown in Fig. 1 in the main text.). **b**, Two-probe resistance across ($R_{2\text{-}3}$, $R_{6\text{-}7}$, and $R_{5\text{-}8}$) and along ($R_{4\text{-}5}$, $R_{2\text{-}7}$, and $R_{3\text{-}6}$) the stripes as a function of n_g in cooldown no. 2. Inset shows the contact configurations for each measurement, where the easy direction (along stripes) is indicated by the grey lines (not to scale). **c**, Four-probe resistance across ("I_{sd}: 5–8; V_{xx}: 6-7" and "I_{sd}: 5–8; V_{xx}: 3-2") and along ("I_{sd}: 3–6; V_{xx}: 4-5", "I_{sd}: 3–6; V_{xx}: 2–7", and "I_{sd}: 2–7; V_{xx}: 4-5") the stripes as a function of n_g in cooldown no. 2.

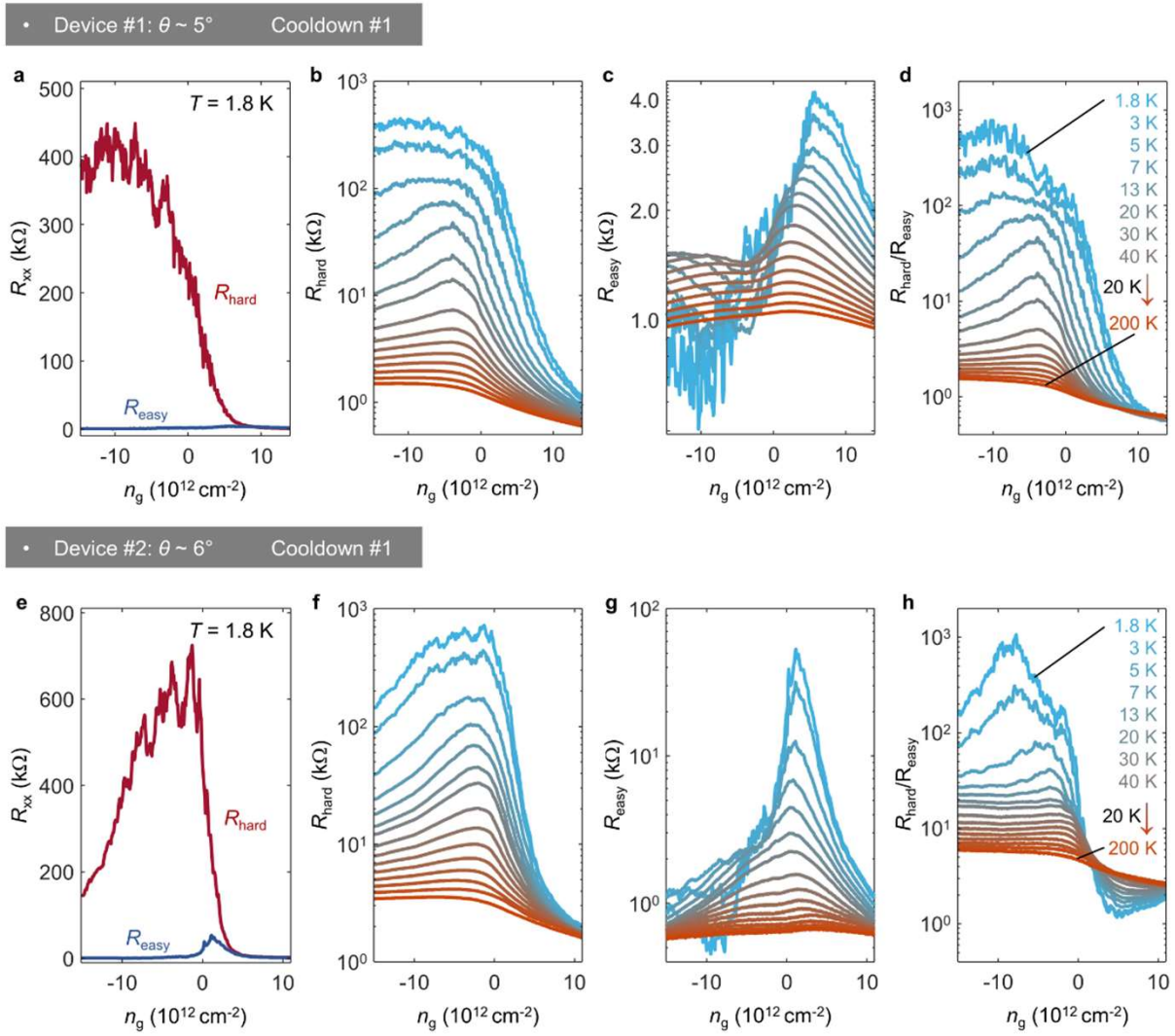

Extended Data Fig. 4 | n_g dependent transport anisotropy for devices no. 1 and no. 2. Four-probe resistance R_{xx} as a function of n_g measured with an excitation current applied along hard and easy directions in linear plots. **a**, data taken for device no. 1 at 1.8 K (the same data as Fig. 1i). **b-d**, R_{hard}, R_{easy}, and R_{hard}/R_{easy} as a function of n_g at different temperatures taken from device no. 1. **e-h**, The same plots for device no. 2.

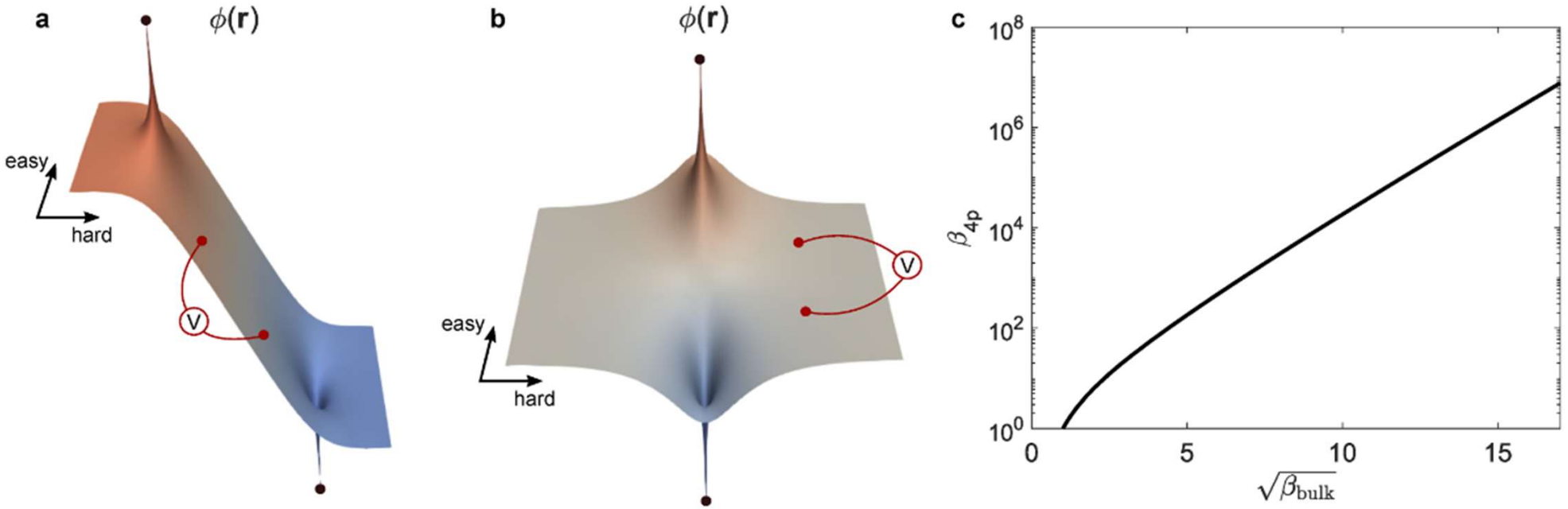

Extended Data Fig. 5 | Electrostatic simulation for the four-probe contact configuration. a & b, Electric potential distribution for contact arrangements corresponding to R_{hard} and R_{easy} four-probe measurements respectively (see Methods). Black dots indicate current contacts that source/sink current. Red dots indicate the placement of voltage contacts. **c**, Predicted four-probe anisotropy $\beta_{4p} \equiv R_{hard}/R_{easy}$ as a function of the intrinsic sheet resistivity anisotropy β_{bulk}. For $\beta_{4p} \approx 1{,}000$, we estimate $\beta_{bulk} \approx 50$.

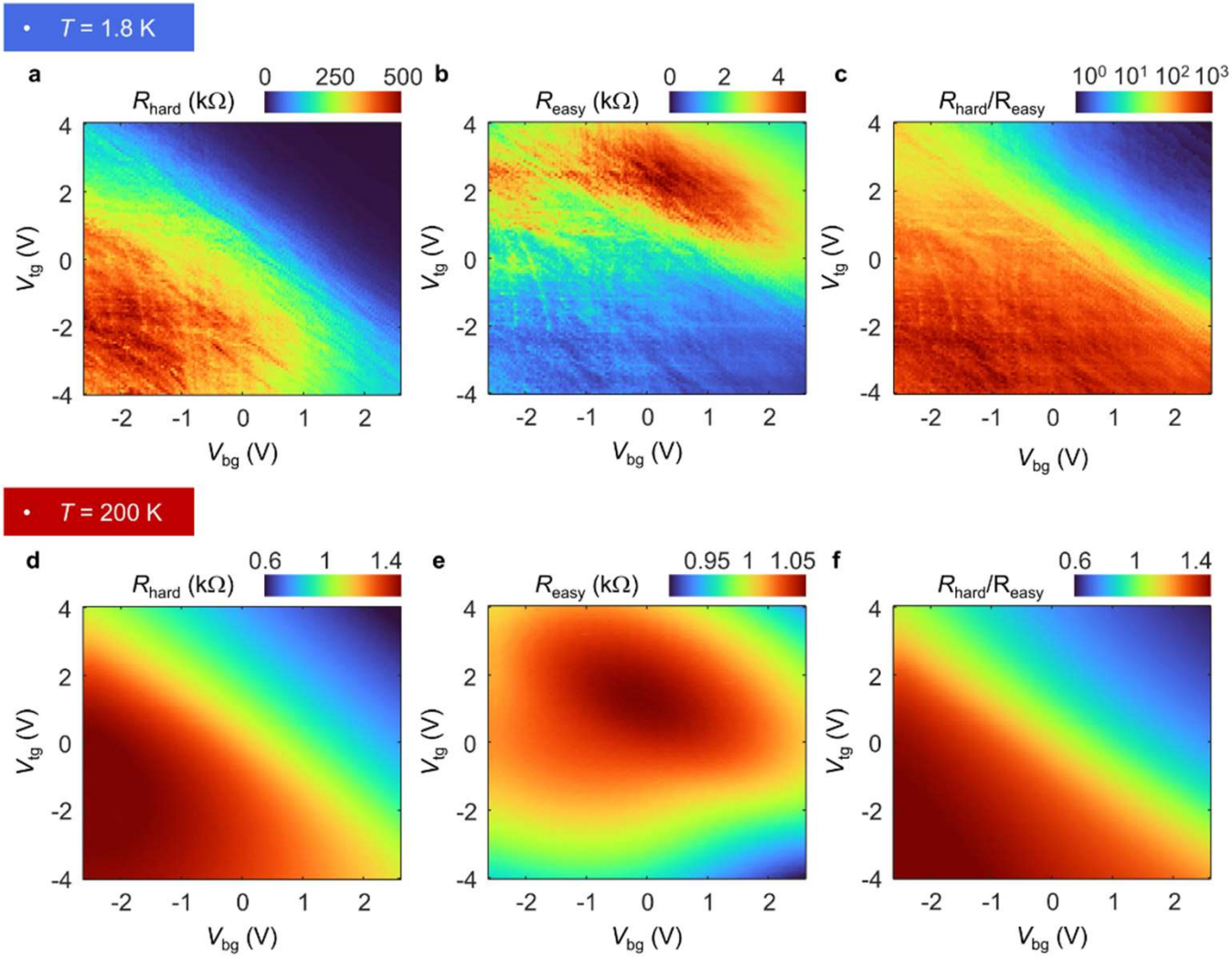

Extended Data Fig. 6 | Dual-gate-dependent transport along hard and easy directions (device no. 1, cooldown no. 1). The four-probe resistance taken at 1.8 K (200 K) along the hard and easy directions were shown in **a** (**d**) and **b** (**e**), respectively. R_{hard}/R_{easy} at 1.8 K (200 K) is shown in **c** (**f**).

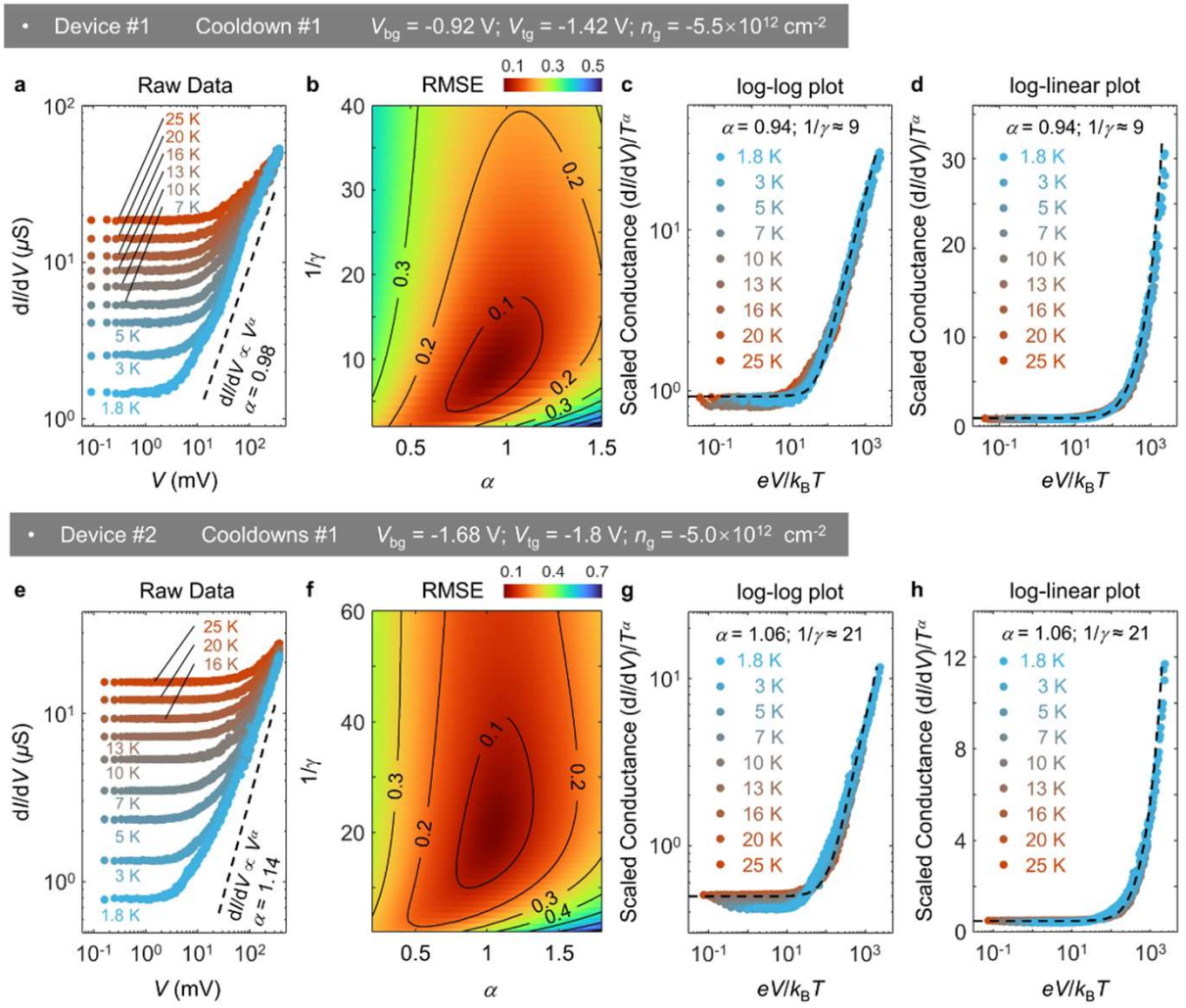

Extended Data Fig. 7 | Fitting to the differential conductance data based on the universal scaling formula. a, Raw data for the differential conductance measurements taken in device no. 1 (replotted from Fig. 2d). **b**, 2D map of calculated root-mean-square error (r.m.s.e.) as a function of the fitting parameters, α and γ (see Methods for details). The best fit is obtained by finding the minimal value of r.m.s.e. in this plot, i.e., $\alpha = 0.94$ and $1/\gamma = 9$. **c & d**, Scaled conductance as a function of scaled excitation by assigning $\alpha = 0.94$ in a log–log plot and log-linear plot. The dashed line indicates the fitting result given by the universal formula defined in the Method section. **e-h**, The same fitting plots for device no. 2, using the same raw data shown in Fig. 2f.

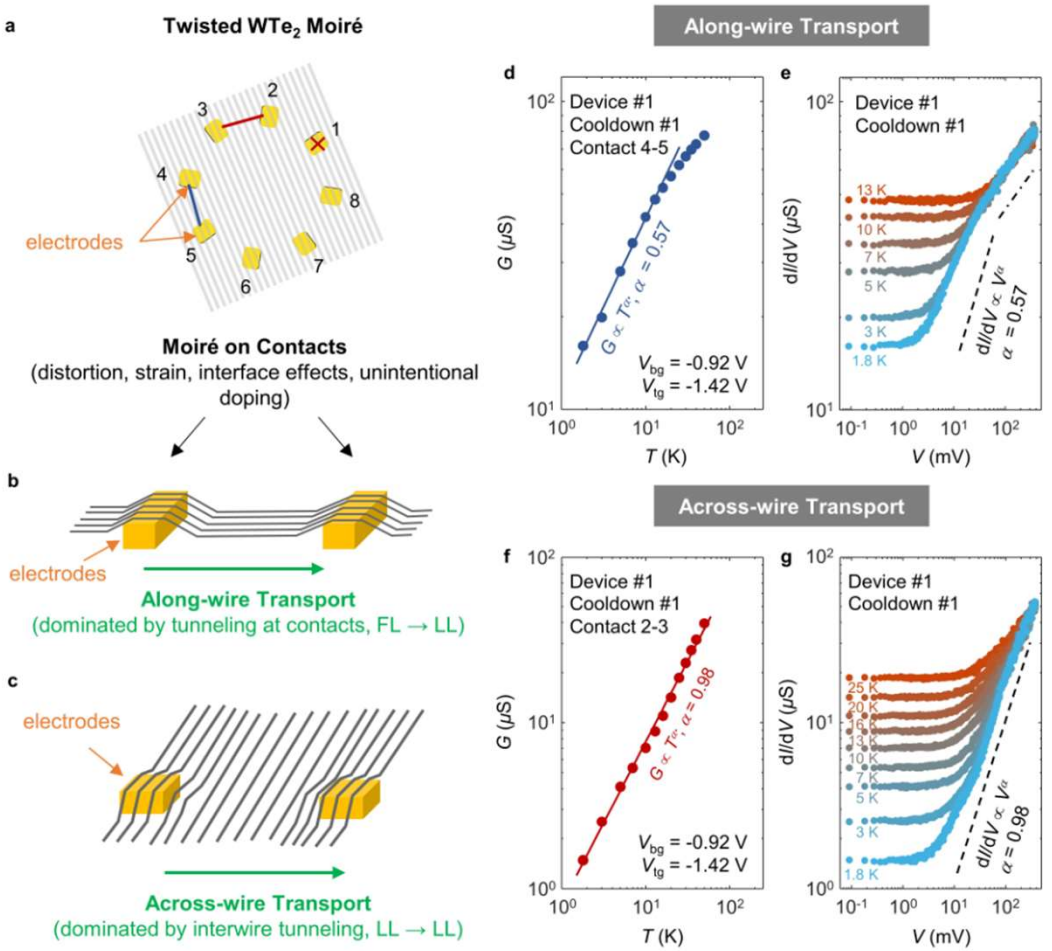

Extended Data Fig. 8 | Comparison between along-wire and across-wire transport. a, Illustration of tWTe$_2$ moiré stripes on the electrodes (top view). **b**, Illustration of transport along wires. At low I, the along-wire transport is dominated by contact resistance, i.e., tunnelling from the metal (FL) to the moiré wires (LL). **c**, Illustration of the across-wire transport, where the dominant resistance is due to interwire tunnelling in the stripe regime (i.e., LL to LL tunnelling). **d**, Along-wire two-probe conductance G as a function of T, plotted in log–log scale at a selected gate parameter. A power-law fit (solid line) to the low T data is shown. **e**, Differential conductance dI/dV taken under the along-wire transport configuration as a function of d.c. bias V at different T. The dashed line indicates a power-law trend. The dot-dash line indicates a deviation from the trend at high bias. Note that distortions, strain, unintentional doing and other interface effects occur at the moiré in the contact regime, which could cause the deviation. **f & g**, the same plot for data taken from the across-wire transport (the same data as Fig. 2c, d), exhibiting a more robust power-law behaviour to higher bias and T. This can be understood as the dominant resistance in the across-wire transport comes from the tWTe$_2$ channel regime, which is more uniform compared to the contact regime. Data were taken from device no. 1 in cooldown no. 1.

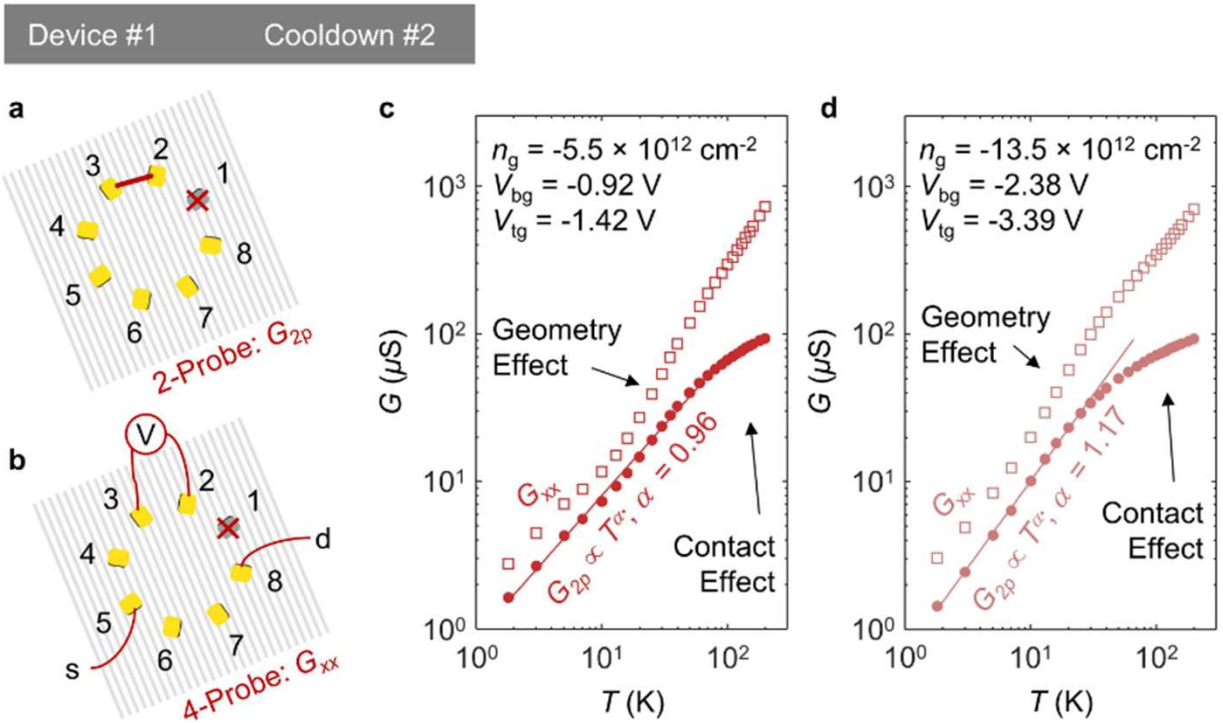

Extended Data Fig. 9 | Comparison of two-probe and four-probe measurements across the wires. Cartoon illustration of (**a**) two-probe (G_{2p}) and (**b**) four-probe (G_{xx}) configurations used for the measurements. **c and d**, G_{2p} and G_{xx} as a function of temperature taken in the hole-doped region ($n_g = -5.5 \times 10^{12}$ cm^{-2} and $n_g = -13.5 \times 10^{12}$ cm^{-2}, respectively). At low T (1.8 K ~ 25 K) the trends of G_{2p} and G_{xx} both follow a power law and match well, demonstrating that the power law is intrinsic to the $tWTe_2$ channel. At high T, the two trends of G_{2p} and G_{xx} deviate from each other, which can be understood as G_{2p} saturates due to contact resistances whereas G_{xx} is strongly affected by the temperature induced changes of anisotropy. The effective geometry factor, important for determining G_{xx}, changes as the sample is tuned from a strongly anisotropic phase at low T to an isotropic phase at high T. The main analyses in this paper are focused on the low T regime. The measurements were performed on device no. 1 in cooldown no. 2.

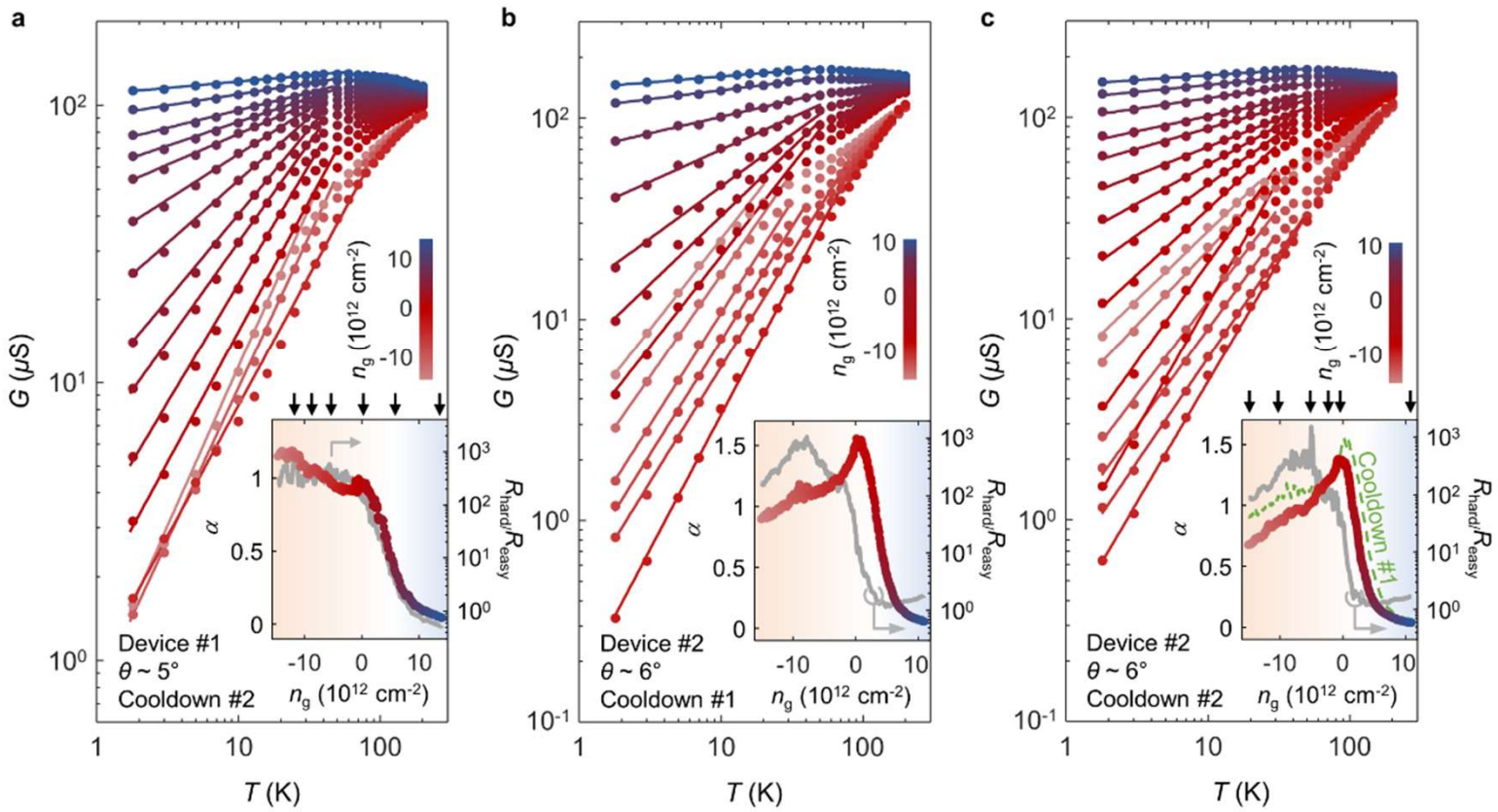

Extended Data Fig. 10 | Gate-tuned anisotropy cross-over. a, The across-wire two-probe conductance $G(T)$ displays a power-law relation ($G \propto T^{\alpha}$) for a wide range of doping for device no. 1 (cooldown no. 2). The colour of the data points encodes n_g, as shown in the colour bar. The solid lines are the power-law fittings, where the extracted exponent α is shown in the inset. The grey line replots the anisotropy ratio. **b**, The same plots for device no. 2 (cooldown no. 1). The grey line replots the anisotropy ratio shown in the inset of Fig. 1h. **c**, The same plots for device no. 2 (cooldown no. 2). Note that data taken from two different cooldowns from device no. 2 shows qualitatively consistent results with only minor quantitative differences (dashed line in the inset of **c** is the exponent α replotted from the inset of **b** for comparison). Arrows to the insets in **a** and **c** indicate the selected n_g, at which the scaling analysis of the differential conductance is performed in Extended Data Figs. 11 and 12, respectively.

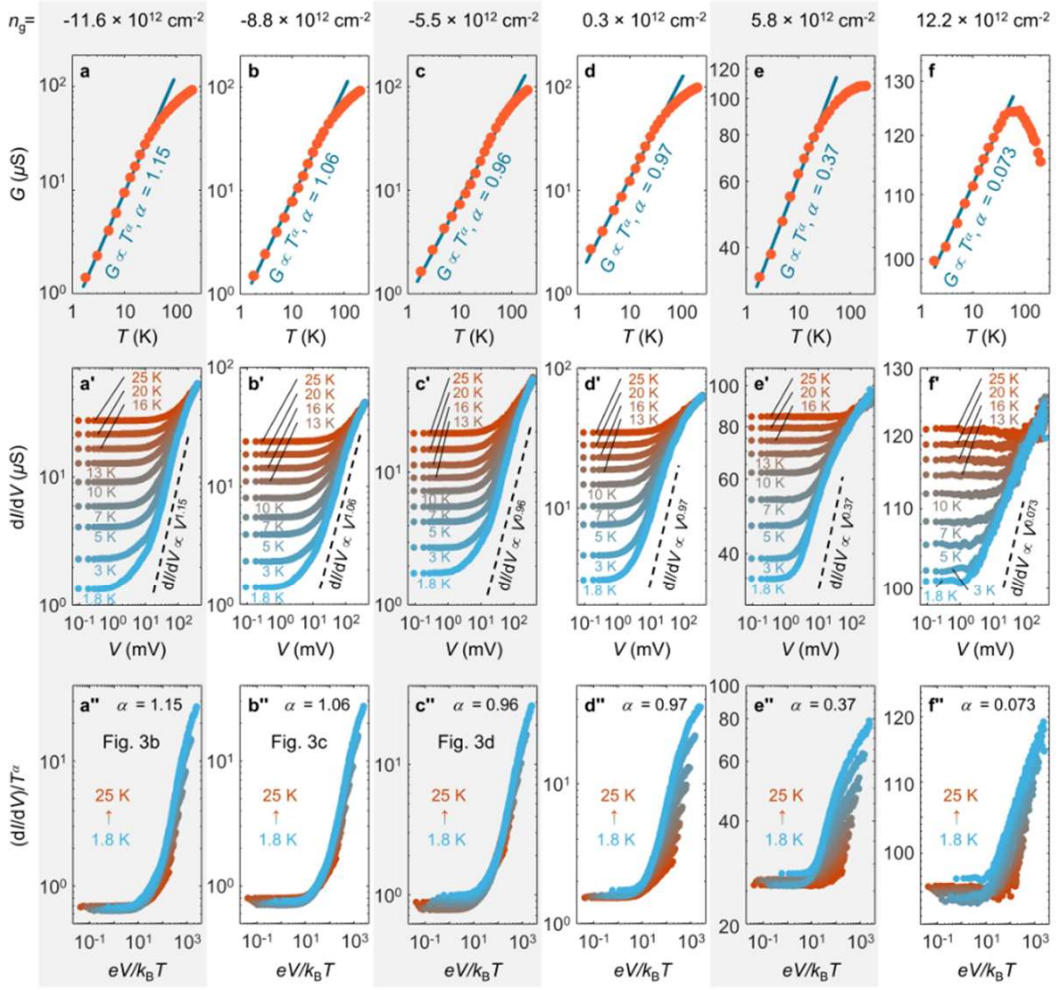

Extended Data Fig. 11 | Additional power-law scaling analysis for device no. 1 (cooldown no. 2). The corresponding n_g for each data set is indicated in the inset of Extended Data Fig. 10a. **a**, Temperature dependent across-wire two-probe conductance $G(T)$ taken at the indicated n_g. The solid line is the power low fit. **a'**, Bias dependent differential conductance taken at the same n_g under different T. The dashed line indicates the power-law trend with the same exponent α extracted in **a**. **a''**, the same data in **a'**, but replotted as scaled differential conductance $(dI/dV)/T^\alpha$ *v.s.* scaled bias eV/k_BT. Other panels are the same plots for different n_g. As seen in the plots, in the hole side (**a**-**c**) the data generally follows a power law very well, whereas near charge neutrality (**d**) and in the electron side (**e**), deviations start to develop at high bias. In the highly electron-doped region (**f**), dI/dV and G vary only a little bit ($\alpha \approx 0$) with changing both V and I, hence the behaviour is approximately ohmic. Data used for Figs. 3b-d are indicated in the lowest panel.

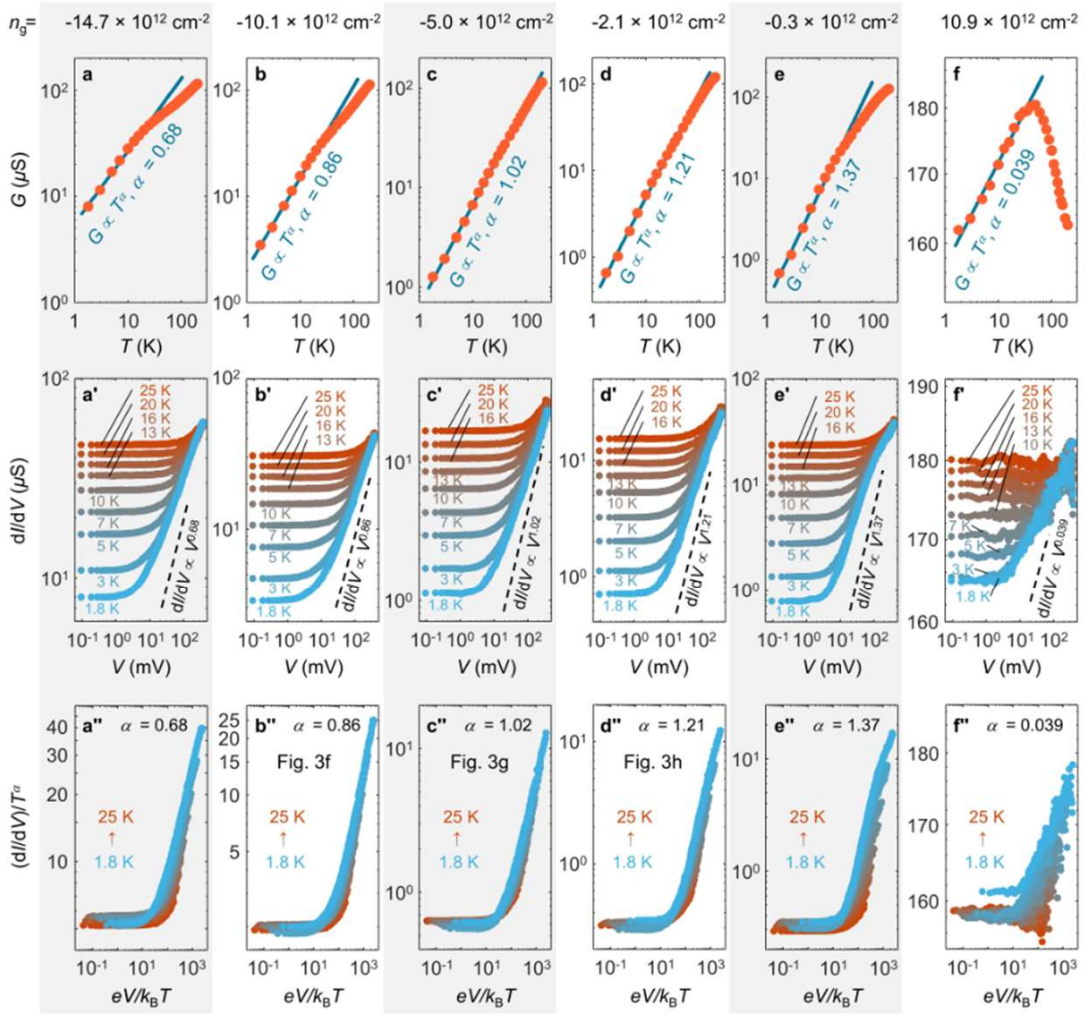

Extended Data Fig. 12 | Additional power-law scaling analysis for device no. 2 (cooldown no. 2). The corresponding n_g for each data set is indicated in the inset of Extended Data Fig. 10c. **a**, Temperature dependent across-wire two-probe conductance $G(T)$ taken at the indicated n_g. The solid line is the power low fit. **a'**, Bias dependent differential conductance taken at the same n_g under different T. The dashed line indicates the power-law trend with the same exponent α extracted in **a**. **a''**, the same data in **a'**, but replotted as scaled differential conductance $(dI/dV)/T^\alpha$ *v.s.* scaled bias eV/k_BT. Other panels are the same plots for different n_g. As seen in the plots, in the hole side (**a**-**d**) the data generally follows a power law very well, whereas near charge neutrality (**e**), deviations start to develop at high bias. In the highly electron-doped region (**f**), dI/dV and G vary only a little bit ($\alpha \approx 0$) with changing both V and T, hence the behaviour is approximately ohmic. Data used for Figs. 3f–h are indicated in the lowest panel.